

Kinematic inversion of isochronous layers in firn for velocity

Olaf Eisen[†]

Versuchsanstalt für Wasserbau, Hydrologie und Glaziologie (VAW), ETH Zürich, Switzerland

Abstract. This study investigates principle suitability of a kinematic approach to invert the velocity field from internal-layer architecture in firn. Internal layers are isochrones and the depositional age of a layer particle is treated as tracer. The linear system to be inverted takes into account two-dimensional steady-state advection of age and conservation of mass. Different inversion strategies with varying combinations of additional velocity constraints are prescribed, thus covering under- and overdetermined systems. The systems are solved using singular-value decomposition, allowing analysis of the singular-value spectrum, model and data resolution and uncertainties. In addition, inversion results are evaluated by comparing the inverted velocity fields with the synthetic input data. For four different flow scenarios stationary age–depth distributions are created by prescribing horizontal advection as plug flow, a density–depth function, and a spatial variation in accumulation. Three scenarios consider non-divergent flow, one scenario covers longitudinally divergent flow. For almost all inversion strategies realistic results require truncation of the singular spectrum, evident from its structure. Results indicate that some constraints on either horizontal or vertical velocity or their properties along a boundary is necessary. Compared to conventional accumulation estimates the inversion has the advantage that effects of lateral advection are taken into account, thus enabling improved separation of spatial and temporal variations in accumulation.

1. Introduction

Internal layering is widely observed by radar sounding in cold firn and ice, on high alpine and polar glaciers as well as ice sheets. Layer architecture results from the interplay of spatio-temporal variation of surface accumulation, bottom melting, and advection caused by ice dynamics. Most layers are isochrones, i.e. of equal age. Whereas age information retrieved from ice cores is only representative for the immediate vicinity of the drilling location, the layer architecture provides a spatial picture. It represents an integrated view of the temporal evolution of an ice mass.

Several studies exploited this property to enhance the view of past and understand present conditions. The most simple application is the one-dimensional direct inversion of layer depth and density distribution for accumulation, covering shallow depth and a view millennia at most (see *Annals of Glaciology* 39 and 41, and references therein, for a summary of studies). However, effects of advection are not considered and introduce errors in the inverted accumulation. Recently, Arcone and others [2005] used an accumulation rate model to investigate how accumulation rate anomalies and ice speed affect stratigraphic variations of internal lay-

ers. Other approaches utilize forward modeling of the whole ice column and least-squares technique to solve for the accumulation rate by minimizing differences between calculated and measured internal layer architecture [Siegert and others, 2003; Jacobel and Welch, 2005]. Parrenin and others [2005] gave analytical solutions for observed layer stratigraphy, depending on accumulation, flow field, and ice thickness. Of special interest are the inversion of flow trajectories to improve firn and ice-core dating and separate spatial from temporal variations. Based on observed thickness anomalies between isochrones, Leonard and others [2004] quantified the effect of a high-accumulation region upstream of the Vostok ice core on the paleoclimatic reconstruction. Morse [1997] attempted to iteratively solve a non-linear least-squares minimisation problem to invert the surface velocity field at Taylor Dome for ice rheology and flow parameters. Waddington and others [2004] invert a forward model for calculating surface height, particle paths, and internal layer shapes, based on layer architecture, which they apply to the area around Taylor Dome.

In this study I present an attempt to kinematically invert the observed layer architecture in firn, i.e. the age–depth distribution, to determine horizontal and vertical velocities. The direct inversion of the flow field from internal layers in the firn column with variable density poses a problem that has

[†]Also at Alfred-Wegener-Institut für Polar- und Meeresforschung, Bremerhaven, Germany

not been investigated so far. Because of the variable density, the modeling of firn rheology is much more difficult than that of solid ice. Studies concerned with deeper layers (below a few hundred meters depth) therefore usually consider density to be constant over the whole ice column. The kinematic approach has the advantage that no assumptions about firn rheology are needed.

2. Inverting Tracer Fields for Velocity

The dispute in the oceanographic community on the question “Can a tracer field be inverted for velocity?”, as formulated by Wunsch [1985] two decades ago, showed that it is in principle possible. Without going into details here it can be said that useful information can be extracted from a tracer distribution about the underlying flow field, even for underdetermined problems. A number of physical and chemical parameters can be used as tracers in ice masses. Of particular interest is the age of deposition of a certain material particle at the ice-sheet surface, hereafter simple referred to as age. In comparison to physical or chemical tracers like isotopic composition or aerosols, age can definitely be considered a conservative tracer, in the sense that it is neither subject to diffusion nor reaction. In the context of ice-core deep drilling for the purpose of paleoclimate research, glaciological applications mainly focused on forward modeling of this tracer under estimated environmental and dynamical conditions [e.g. Nereson and Waddington, 2002; Clarke and others, 2005]. Typical application examples are the reconnaissance of suitable drilling sites, or ice-core dating by flow modeling.

Before applying a kinematic inversion scheme to real field data, it is important to understand its strengths and identify pitfalls. This can best be achieved by creating synthetic data to test algorithms, as all parameter fields are known beforehand. I use a simple prognostic forward model to create synthetic stationary age distributions under prescribed conditions for different flow scenarios of varying complexity for the upper 100 m of the ice sheet, the firn column. Subsequently I apply a diagnostic inversion model to the synthetic age distribution to invert for the velocity field. The inversion is based on the singular-value decomposition (SVD). SVD has several advantages over other schemes, like e.g. least squares, especially in terms of analysing the inversion results [as summarized, for instance, by Wunsch, 1996]. Various combinations of boundary conditions and matrix weighting for the different flow scenarios are used as inversion strategies, covering the full range from under- to overdetermined systems. Comparison of reference velocities calculated by the prognostic model with the inverted velocities then provides a means to evaluate the performance and reliability of the SVD inversion strategies. After introducing the flow scenarios, the basic inversion formalism and strategies in this section, the main part of the paper exploits SVD peculiarities for interpreting the results.

2.1. Kinematic Equations

The approach presented here is based on a kinematic consideration of the firn volume, therefore the fundamental equations for conservation of energy and impulse are not taken into account. In general, the distribution of any tracer in a medium can be described by an advection-diffusion equation. (Details on the tracer transport and formulation in ice sheets are extensively discussed by Clarke and others [2005].) In our case, the corresponding tracer is depositional age, $A = A(\mathbf{r}, t)$, a non-diffusive property, which obeys

$$\partial_t A + \mathbf{v} \cdot \nabla A = 1. \quad (1)$$

All calculations are carried out in two-dimensional (2D) space, $\mathbf{r} = (x, z)$ (z positive and increasing downward). ∂_t denotes the partial derivative with respect to the subscripted variable, here time t . Equation (1) is sometimes referred to as age equation [Hindmarsh and others, 2005, e.g.]. The right-hand side represents a source term and is responsible for the actual aging of the firn with time.

The second governing equation is the conservation of mass,

$$\partial_t \rho + \nabla \cdot (\rho \mathbf{v}) = 0. \quad (2)$$

where $\rho = \rho(\mathbf{r}, t)$ is the density. These two equations form the fundamental system of linear equations used in the forward model and the inversion.

2.2. Assumptions and boundary conditions

A number of assumptions are employed for the sake of simplicity, however without depreciating the general applicability of the inversion. The considered firn volume extends from the surface ($z = 0$) to an arbitrary depth ($z = z_{max}$). The density distribution is taken to be laterally homogeneous and time-independent, $\partial_x \rho = \partial_y \rho = \partial_t \rho = 0$ (Sorge’s law), but depth-dependence is maintained ($\partial_z \rho \neq 0$). This assumption is well justified on a regional scale for ice-sheet plateaus [e.g. Frezzotti and others, 2004; Richardson-Näslund, 2004; Rotschky and others, 2004; Arcone and others, 2005], but has to be considered with care on cold alpine glaciers. Note that the depth-dependency of density is a prominent difference to the incompressibility assumption often used in ice-sheet modeling. Time-dependence of equations (1) and (2) is maintained in the prognostic forward model. The system of equations to be inverted, however, is formulated in a time-independent way so that $\partial_t(\cdot) = 0$, as the forward model produces a steady-state age distribution as output, where (\cdot) denotes any term to be differentiated.

No forces appear in the above equations, simplifying matters such that the upper boundary can be taken as a horizontal surface, i.e. parallel to x . Position and direction of scalar and vector quantities then always refer to this surface. (For illustrative comparison see Arcone and others [2005]: consider a radargram which contains records of the reflector depth with respect to the relative surface. Only during data processing a topographic correction is applied.) The kinematic boundary

condition at the surface is $w(x, z = 0) = \dot{b}(x)/\rho_0$, where $\dot{b}(x)$ is the surface accumulation and $\rho_0 = \rho(z = 0)$ is the density at the surface. Additional constraints are introduced later, primarily as prescribed velocity properties.

2.3. Prognostic forward model

The forward model runs under prescribed stationary allocations of density, horizontal velocity, and accumulation on an ordinary grid, discretised with finite differences. It calculates the vertical velocity from the combined effect of accumulation at the surface, advection, and densification, and yields the synthetic age–depth distribution. Starting from an initial laterally homogeneous, vertically increasing age distribution, the prognostic model runs in a transient mode until a steady state is reached. Details on grid parameters are listed in Table 1. The age–depth distribution constitutes the essential output, which is passed on to the inversion model. The prescribed horizontal velocities \mathbf{u}^{ref} and calculated vertical velocities \mathbf{w}^{ref} of the forward model are defined for all grid points. We further on use refer to them as the reference-velocity field, denoted by the superscript *ref*, against which the inverted velocity field is compared.

2.4. Linear system for inversion

The time-independent forms of equations (1) and (2) read

$$u\partial_x A + w\partial_z A = 1 \quad (3a)$$

$$\rho\partial_x u + \rho\partial_z w + w\partial_z \rho = 0. \quad (3b)$$

The discretisation schemes for solving this linear system on a triplex-staggered grid are taken in an adapted form from Fiadeiro and Veronis [1982] and Wunsch [1985]. The input fields of age and density are prescribed on a rectangular grid, the *A*-grid, with a grid spacing of Δx and Δz in *x*- and *z*-direction, respectively (Fig. 1). The *A*-grid has $I \times K$ nodes. The grid nodes representing *u* and *w* (*u*- and *w*-grid) are shifted by half the grid spacing in the horizontal and vertical direction, respectively, relative to the nodes on which the input parameters for age and density are prescribed (Fig. 1). Application of staggered-grid differences to (3) leads to a discrete system, which for a unit cell (Fig. 1a) can be expressed as

$$\begin{pmatrix} c_{i,k}^\alpha & c_{i+1,k}^\beta & c_{i,k}^\gamma & c_{i,k+1}^\delta \\ c_{i,k}^\kappa & c_{i+1,k}^\lambda & c_{i,k}^\mu & c_{i,k+1}^\nu \end{pmatrix} \begin{pmatrix} u_{i,k} \\ u_{i+1,k} \\ w_{i,k} \\ w_{i,k+1} \end{pmatrix} = \begin{pmatrix} 1 \\ 0 \end{pmatrix}$$

Detailed expressions of the staggered-grid differences and variables $\{c_{i,k}^{\alpha,\dots,\nu}\} = f(A, \rho)$ are omitted for brevity. Whereas all values of $u_{i,k}, w_{i,k}$ within the dashed region in Fig. 1, the solution domain, are implicit functions of the prescribed variables *A* and ρ , their values on the boundaries cannot be fully determined. However, this formulation has the advantage that no other specific conditions are necessary at the boundaries of the SVD domain. The number of unknown

variables *u* and *w* differs along a certain dimension (*x* or *z*) within the solution domain: $n_u^x = I - 1$, $n_u^z = K - 2$, $n_w^x = I - 2$, $n_w^z = K - 1$. The total number of elements of each variable within the solution domain are $n_u = n_u^x n_u^z$ and $n_w = n_w^x n_w^z$. Defining the following vectors and matrix,

$$\begin{aligned} \mathbf{d} &= (1, 1, \dots, 0, 0)^T \in \mathcal{R}^M, M = 2n_u^z n_w^x, \\ \mathbf{v} &= (\{u_{i,k}\}, \{w_{i,k}\})^T \\ &= (\mathbf{u}^T, \mathbf{w}^T)^T \in \mathcal{R}^N, N = n_u + n_w, \\ \mathbf{M} &= (\{c_{i,k}^\alpha\}, \dots, \{c_{i,k}^\nu\}) \in \mathcal{R}^{M \times N}, \end{aligned} \quad (4)$$

allows one to set up the matrix equation

$$\mathbf{M}\mathbf{v} = \mathbf{d}. \quad (5)$$

In standard terms, \mathbf{d} represents the data in data space \mathcal{R}^M and \mathbf{v} represents the model parameters in model space \mathcal{R}^N . *M* is the number of (known) equations, *N* is the number of unknowns, in our case the velocities within the solution domain¹. The relationship of model parameters and data is described by the model matrix \mathbf{M} , sometimes referred to as the data kernel [Menke, 1989].

3. Singular Value Decomposition

3.1. Basic principles

The SVD of a matrix \mathbf{M} is a generalisation of the spectral decomposition of a square to a rectangular matrix, which always exists. Here we apply SVD to calculate the pseudo-inverse (or generalised inverse) of \mathbf{M} , mainly following the notation of Wunsch [1996]. Any rectangular matrix \mathbf{M} can be decomposed into a factorisation of the form

$$\mathbf{M} = \mathbf{U}\mathbf{\Lambda}\mathbf{V}^T, \quad (6)$$

where \mathbf{U} and \mathbf{V} are both unitary rectangular matrices, $\mathbf{U} \in \mathcal{R}^{M \times M}$, $\mathbf{V} \in \mathcal{R}^{N \times N}$, and \mathbf{V}^T denotes the transpose of \mathbf{V} . The generally non-square matrix $\mathbf{\Lambda} \in \mathcal{R}^{M \times N}$ contains the singular values (square root of eigenvalues) of \mathbf{M} in decreasing order on the main diagonal, $\Lambda_{ij} = \delta_{ij} \lambda_i$, with the Kronecker symbol δ_{ij} . The matrix \mathbf{V} contains a set of orthogonal input base-vectors of \mathbf{M} , spanning the *N*-dimensional model (or inverse solution) space, whereas the matrix \mathbf{U} contains a set of orthogonal output base-vectors spanning the *M*-dimensional data (or observation) space. The number *R* of non-zero singular values is the rank of \mathbf{M} . If some singular values are zero or $M \neq N$, one or more of the rows or columns of $\mathbf{\Lambda}$ must all be zeros. One can then drop those columns of \mathbf{U} and \mathbf{V} that are multiplied by zeros only, thus reducing the matrices in (6) to the expression

$$\mathbf{M} = \mathbf{U}_R \mathbf{\Lambda}_R \mathbf{V}_R^T, \quad (7)$$

where the subscript *R* indicates the number of columns, with $\mathbf{U}_R \in \mathcal{R}^{M \times R}$ and $\mathbf{V}_R \in \mathcal{R}^{N \times R}$. $\mathbf{\Lambda}_R$ is the submatrix

¹Note the arbitrary usage of *M* and *N* in the literature.

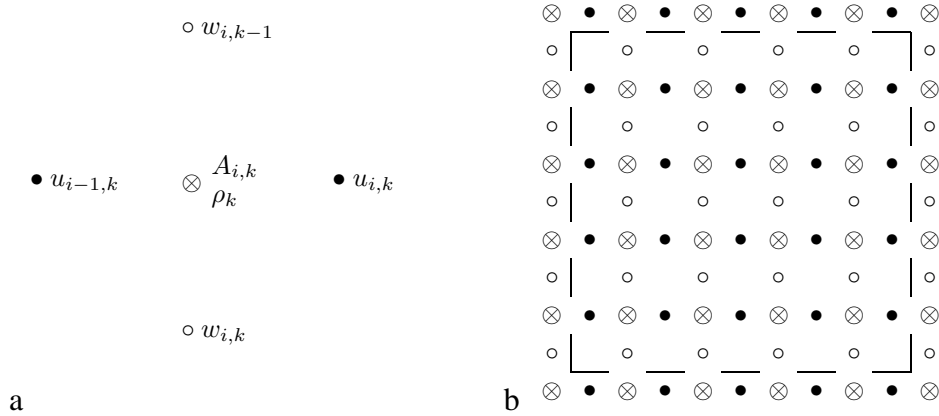


Figure 1. (a) Unit-cell scheme of the numerical grid used for solving the linear system of equation (3). (b) Scheme of the triplex-staggered numerical grid for $I = K = 6$. The solution domain is bounded by the dashed line. The uppermost row corresponds to the surface. Distance between congenerous nodes is Δx and Δz , between nodes of different type $\Delta x/2$ and $\Delta z/2$ in the horizontal and vertical direction, respectively.

of $\mathbf{\Lambda}$ with non-vanishing singular values. It can be shown [Wunsch, 1996] that $\mathbf{V}_R \mathbf{\Lambda}_R^{-1} \mathbf{U}_R^T$ is the pseudo-inverse of \mathbf{M} , which we use to solve (5) for the unknown model vector, the solution

$$\mathbf{v} = \mathbf{V}_R \mathbf{\Lambda}_R^{-1} \mathbf{U}_R^T \mathbf{d}, \quad (8)$$

where $\mathbf{\Lambda}_R^{-1}$ is the inverse of $\mathbf{\Lambda}_R$, i.e. with λ_i^{-1} on the main diagonal ($\lambda_i \neq 0$). The above expressions for \mathbf{M} , \mathbf{U} , and \mathbf{V} define four spaces: the model range $\mathbf{V}_R \in \mathcal{R}^{N \times R}$ (column space of \mathbf{M}), the model nullspace $\mathbf{V}_0 \in \mathcal{R}^{N \times (N-R)}$, the data range $\mathbf{U}_R \in \mathcal{R}^{M \times R}$ (row space of \mathbf{M}), and the data nullspace $\mathbf{U}_0 \in \mathcal{R}^{M \times (M-R)}$. Depending on the size of M , N , and R , not of all of these spaces need to be coexistent. Conditions for existence, terminology, and combinations are listed in the appendix. If there is a data nullspace \mathbf{U}_0 ($R < M$), and if the data have components in it, then it will be impossible to fit the data exactly. The residual norm will then be different from zero. On the other hand, if the model has components in the model nullspace \mathbf{V}_0 ($R < N$), then it will be impossible to determine the model exactly. In that case the model solution can be presented as a sum of the particular solution (8), which contains only range vectors, and an arbitrary homogeneous solution $\mathbf{V}_0 \boldsymbol{\alpha}$ of (5) of $(N - R)$ vectors in the model nullspace with coefficients $\boldsymbol{\alpha}$, about which the equations provide no information.

The SVD is related to the least-square approach. All of the structure imposed by SVD is also present in least-squares solutions. One commonality is that the SVD simultaneously minimises the residual and solution norms (minimum norm property, e.g. Scales and others [2001, p. 66]). However, the SVD solution generalises the least-square solution to the case where the matrix inverses of $\mathbf{M}^T \mathbf{M}$ or $\mathbf{M} \mathbf{M}^T$, the simplest forms, do not exist, for instance if the system is not full rank [Wunsch, 1996, 157f]. An important advantage for the application of SVD and the interpretation of the solution

is that only a single algebraic formulation is necessary, irrespective to over-, under-, or just-determined systems. The SVD provides its control over the solution norms, uncertainties, and covariances through choice of the effective rank $\hat{R} \leq R$, which leads to the so-called truncated SVD, demonstrated later. The truncated form makes a clear separation between range and nullspace in both solution and residual spaces.

3.2. Resolution

A useful peculiarity of the SVD is that it provides direct access to the resolution of mapping model and data spaces (for discussions see Menke [1989, p.62f] and Wunsch [1996, p.165]). The model resolution matrix, defined as

$$\mathbf{T}_V = \mathbf{V}_R \mathbf{V}_R^T, \quad (9)$$

determines the relationship between the general solution and the particular solution. If no model nullspace exists ($R = N$), the general and particular solution are equal. Then $\mathbf{T}_V = \mathbf{I}_N$, the $N \times N$ -dimensional identity matrix, meaning that the model is completely resolved. In the opposite case, non-zero terms will appear off the main diagonal in (9), so only averages of some model parameters can be resolved. Analogously, the data resolution matrix

$$\mathbf{T}_U = \mathbf{U}_R \mathbf{U}_R^T \quad (10)$$

provides information on how well the observed data is reproduced by the generalised inverse. Both resolution matrices are functions of the data kernel \mathbf{M} and the a-priori information (the model) of the problem. They do not depend on the model parameters \mathbf{v} and the data \mathbf{d} .

3.3. Error covariance and uncertainty

Every estimate of model parameters \mathbf{v} is subject to uncertainties. Using an estimated \mathbf{v} in (5) yields a data vector which differs from the true \mathbf{d} by some residual noise, referred to as \mathbf{n} . The covariance of the estimated model parameters depends on the noise covariance $\mathbf{R}_{\mathbf{nn}}$ (the second-moment matrix of \mathbf{n}). It can be shown to be [Wunsch, 1996, p.143]

$$\mathbf{C}_{\mathbf{vv}} = \mathbf{V}_R \mathbf{\Lambda}_R^{-1} \mathbf{U}_R^T \mathbf{R}_{\mathbf{nn}} \mathbf{U}_R \mathbf{\Lambda}_R^{-1} \mathbf{V}_R^T. \quad (11)$$

In the case of uncorrelated uniform variance σ_n^2 of the data (11) simplifies to

$$\mathbf{C}_{\mathbf{vv}} = \sigma_n^2 \mathbf{V}_R \mathbf{\Lambda}_R^{-2} \mathbf{V}_R^T. \quad (12)$$

The covariance of the model parameters arises from noise present in the data and generates uncertainty in the coefficients of the model range vectors. Data covariance is thus mapped onto model covariance. To obtain the complete solution uncertainty $\mathbf{P}_{\mathbf{vv}}$ of the model parameters, the influence of the missing nullspace contribution has to be taken into account as well. It follows as [Wunsch, 1996, p.151]

$$\mathbf{P}_{\mathbf{vv}} = \mathbf{C}_{\mathbf{vv}} + \mathbf{V}_0 \mathbf{R}_{\alpha\alpha} \mathbf{V}_0^T, \quad (13)$$

where $\mathbf{R}_{\alpha\alpha}$ is the second-moment matrix of the coefficients α of the homogeneous solution. $\mathbf{R}_{\alpha\alpha}$ may be entirely unknown, or an estimate from a-priori information might be available. The uncertainty of the residuals is

$$\mathbf{P}_{\mathbf{nn}} = \mathbf{U}_0 \mathbf{U}_0^T \mathbf{R}_{\mathbf{nn}} (\mathbf{U}_0 \mathbf{U}_0^T)^T. \quad (14)$$

The covariance (11) of the estimated model parameters is very sensitive to small non-zero singular values. Solution variance can be reduced by choosing a $\hat{R} < R$ to exclude small λ_i . Inspecting the singular-value spectrum of the data kernel enables one to choose an appropriate cut-off size for contributing singular values [Menke, 1989, p.122]. This artificial reduction of model- and data-space dimensions leads to rank deficiency, and thus worse resolution, and increased dimensions of the nullspaces, but decreases model covariance. Choosing an effective rank \hat{R} therefore provides a means to trade-off variance and resolution, or solution and residual norm, respectively.

3.4. Scaling and weighting

Weighting is in general used to give more importance to certain observations than to others, mainly to correct for uncertainty. On the other hand, if a system consists of different physical equations, then the varying norm of the equations leads to undesired weighting. The norm of the rows of the linear system (5) are different due to the physical variables involved (age and density). To correct for this effect we first apply row scaling to the matrix \mathbf{M} through the matrix \mathbf{W} . Likewise, the columns of \mathbf{M} are of different norm, so that

we require column scaling after the row scaling by the matrix \mathbf{S} . The linear system (5) is transformed to the scaled space (denoted by \sim),

$$\begin{aligned} \mathbf{W}^{-T/2} \mathbf{M} \mathbf{S}^{T/2} \mathbf{S}^{-T/2} \mathbf{v} &= \mathbf{W}^{-T/2} \mathbf{d} \\ \iff \tilde{\mathbf{M}} \tilde{\mathbf{v}} &= \tilde{\mathbf{d}}, \end{aligned} \quad (15)$$

where \mathbf{W} contains the L_2 norm of each equation (row norm of \mathbf{M}) on the diagonal and has the Cholesky decomposition $\mathbf{W} = \mathbf{W}^{T/2} \mathbf{W}^{1/2}$ [Wunsch, 1996, p.159]. Similarly, \mathbf{S} contains the column norm of the already row-scaled matrix $\mathbf{W}^{-T/2} \mathbf{M}$. The SVD is applied in the scaled space. Back transformation from the scaled to the original space, $\mathbf{v} = \mathbf{S}^{T/2} \tilde{\mathbf{v}}$, then provides the desired solution. Despite the fact that for a full-rank underdetermined (overdetermined) system, row (column) scaling is irrelevant, we always apply both scalings to cover all general cases. In addition to scaling, the use of \mathbf{W} and \mathbf{S} allows a degree of control of the relative norms of solution and residual, as is the case for least squares. Below we will apply a third scaling matrix \mathbf{F} , such that $\mathbf{F}^T \mathbf{S} \mathbf{F}$ instead of \mathbf{S} will be used in (15), and \mathbf{F} contains a-priori information about the covariance of the estimated model parameters \mathbf{v} .

3.5. Separation of mean and variation

The minimum-norm property of the SVD will result in a solution that is smallest, in the sense of being closest to zero. However, as we are rather interested in finding the variations of velocity around an average, it is feasible to consider only the variations of the flow field on a homogeneous background. Hence we separate the mean flow from its spatial variations by

$$\mathbf{v} = \bar{\mathbf{v}} + \mathbf{v}', \quad (16)$$

where $\bar{\mathbf{v}} = (\bar{\mathbf{u}}^T, \bar{\mathbf{w}}^T)^T$ is the mean flow field and $\mathbf{v}' = (\mathbf{u}'^T, \mathbf{w}'^T)^T$ the spatial variation. Separate mean values $\bar{u} = \langle \mathbf{u} \rangle$, $\bar{w} = \langle \mathbf{w} \rangle$ are used for horizontal and vertical velocities, respectively, and $\bar{\mathbf{u}} = \bar{u} \mathbf{i}_{n_u}$, $\bar{\mathbf{w}} = \bar{w} \mathbf{i}_{n_w}$, where \mathbf{i}_n is a vector of length n with all ones. Our linear system (3) can then be reformulated as

$$\mathbf{M} \mathbf{v}' = \mathbf{d}' = \mathbf{d} - \mathbf{M} \bar{\mathbf{v}}. \quad (17)$$

For the rest of the paper we drop the attribute \sim . We assume that separation of mean and variation and subsequent scaling have been applied prior to SVD. The results are then discussed in terms of the variational component of the velocity field \mathbf{v}' , as well as the complete velocity field \mathbf{v} .

4. Simulations and Inversion

4.1. Scenarios

Different synthetic scenarios of flow are created with the forward model, with physical parameters chosen such as to mimic real conditions. The horizontal flow field \mathbf{u}^{ref} is prescribed. A Gaussian variation in surface accumulation $\hat{b}(x)$

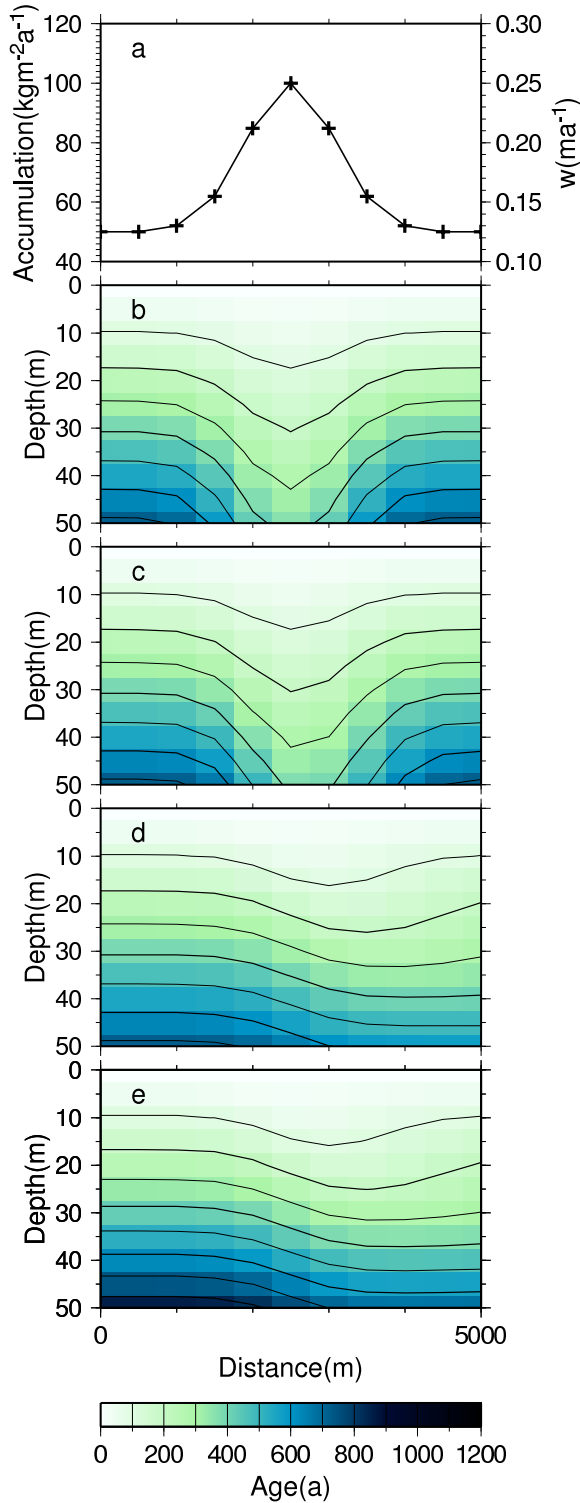


Figure 2. Accumulation forcing (a) and resulting age-depth distributions using different horizontal velocities of scenario (b) NF, (c) SF, (d) MF, (e) MDF for the upper 50 m of the firn column (Table 1). Horizontal flow is from left to right. Crosses in (a) indicate position of nodes on A -grid, scale on the right is vertical velocity at the surface.

Table 1. Simulation parameters

Scenario	\bar{u}^{ref} (m a ⁻¹)	$\partial_x u^{ref}$ (a ⁻¹)	u^{ref}
NF	0	0	0
SF	1	0	0
MF	10	0	0
MDF	10	$4 \cdot 10^{-5}$	$\neq 0$

dimension	min	max	increment
<i>Prognostic Forward Model</i>			
x	0	5 km	100 m
z	0	100 m	1 m
<i>SVD inversion</i>			
x	0	5 km	500 m
z	0	50 m	5 m

NF: no flow; SF: slow flow; MF: moderate flow; MDF: moderate divergent flow with a 20% increase in u over the x -domain. \bar{u} is constant over the complete domain.

is superimposed,

$$\dot{b}(x) = \dot{b}_0 \left(1 + \exp \left[-\frac{(x - x_\mu)^2}{x_\sigma^2} \right] \right) \quad (18)$$

where $\dot{b}_0 = 50 \text{ kg m}^{-2} \text{ a}^{-1}$ is the background accumulation, a value typical for the Antarctic plateau. The maximum accumulation occurs at $x_\mu = 0.5(x_{min} - x_{max})$, the center of the x -domain, with $\dot{b}(x_\mu) = 2\dot{b}_0$. $x_\sigma = x_\mu/6$ determines the width of the distribution (Fig. 2a). Following Richardson and Holmlund [1999], density is parameterised as

$$\rho(z) = \rho_i + (\rho_0 - \rho_i)e^{-c_\rho z}. \quad (19)$$

$\rho_0 = 400 \text{ kg m}^{-2} \text{ a}^{-1}$ and $\rho_i = 900 \text{ kg m}^{-2} \text{ a}^{-1}$ represent values for the density at the surface and of solid ice, respectively, and $c_\rho = 0.05$. This density distribution is likewise typical for different snow regimes in Antarctica.

We consider four different flow regimes of firn with prescribed horizontal velocity field (Table 1). In the most simple case, no horizontal advection takes place (scenario “no flow”, NF). This could be considered the case for a broad ice dome or along an ice divide. The other cases consider constant slow (SF) $\bar{u} = 1 \text{ m a}^{-1}$ and constant moderate flow (MF), $\bar{u} = 10 \text{ m a}^{-1}$, which are also typical for polar ice sheets [Xiaolan and Jezek, 2004; Bamber and others, 2000] or high-altitude alpine glaciers [e.g. Lüthi and Funk, 2001; Schwerzmann and others, 2006]. For these three scenarios the prescribed velocity variation $u^{ref} = \mathbf{0}$. For the moderate velocity of $\bar{u} = 10 \text{ m a}^{-1}$, a fourth scenario considers

divergent flow (MDF) of the form $u(x) = \bar{u} + c_u(x - x_\mu)$, with c_u such that $u(x)$ increases by 20% from $0.9\bar{u}$ to $1.1\bar{u}$ over the x -domain, and thus $\mathbf{u}^{ref} \neq \mathbf{0}$. As a scenario with non-constant horizontal velocities is the most likely case to encounter in reality, it will be in the special focus of the later analysis. Typical speeds for fast ice-stream flow are not taken into account in this feasibility study, as ice dynamics become increasingly important.

The forward model is implemented on a grid spanning 5 km in the horizontal and 100 m the vertical direction, containing 51×101 nodes (Table 1). This volume suffices to cover the firn region of cold polar or high-altitude sites and also comprises characteristic length scales of variations in accumulation. The scenarios clearly show how the varying horizontal advection affects the resulting age-depth distribution (Fig. 2). For scenario SF, the effect of the accumulation variation tapers off before an affected ice particle leaves the model domain. For both MF-scenarios, advection is larger, so the accumulation effect is still present at the model out-flow boundary.

4.2. Constraints and inversion strategies

A standard approach to determine the parameters of a physical model, assumed to be a compatible description of a system, is to minimise an objective function which gauges the misfit between measurements and model results. Model physics are usually enforced as constraints on the minimisation in the form of exact equations, so-called hard constraints [e.g. Wunsch, 1996]. For ice-flow modeling this was for instance presented by MacAyeal [1993] in the case of estimating the basal friction of an ice stream and applied to real data later [MacAyeal and others, 1995; Vieli and Payne, 2003; Joughin and others, 2004; Larour and others, 2005]. In addition to the basic physical description of a system, certain aspects of a solution like structure, norm, or boundary values are also sometimes known a-priori. This information is valuable and helps restricting the in general non-unique solutions of inversions. It can either be included as a hard constraint in the objective function, or as a soft constraint, for instance in trading the norm of the solution vs. the norm of the noise by weighting, leading to tapered or damped least-squares solutions [Menke, 1989, p.52]. Although the SVD does not explicitly employ an objective function, hard and soft constraints can likewise be imposed.

Each of the different sets of constraints applied in the following exercises with synthetic scenarios can in reality also be determined from measured data. For the problem I address here, the flow and deformation of firn, one usually has a rough idea what the flow field at the surface looks like. Horizontal surface velocities can be measured directly (e.g. GPS surveying of stakes) or indirectly (e.g. InSAR observations). Here, the reference velocity field \mathbf{v}^{ref} represents possible measurements, and thus provides a-priori information about various velocity characteristics. It is thus possible to prescribe different parts of the horizontal velocity at the

surface ($k = 0$),

$$u_{i,0} = u_{i,0}^{ref}, \quad (20)$$

or properties of the derivative, e.g. uniform, divergent, or convergent flow,

$$u_{i-1,0} - u_{i,0} = \Delta_x u_{i,0}^{ref}. \quad (21)$$

Distribution of horizontal velocities with depth are deducible from measurements of borehole deformation, enabling us to also use $k \neq 0$ in (20) for values at depth at the borehole location ($i = i_b$), but also to infer properties on shearing,

$$u_{i_b,k} = u_{i_b,k}^{ref}, \quad (22)$$

$$u_{i_b,k-1} - u_{i_b,k} = \Delta_z u_{i_b,k}^{ref}. \quad (23)$$

The case $\Delta_z u_{i_b,k}^{ref} = 0$, i.e. constant horizontal velocity along the vertical, is commonly referred to as plug flow and will be used later.

Not only can horizontal deformations be deduced from borehole deformation, it is also possible to directly determine the vertical velocities by different methods. One way is to observe the movement of markings in a borehole wall [e.g. Schwerzmann and others, 2006]. This provides similar information for the vertical velocities,

$$w_{i_b,k} = w_{i_b,k}^{ref}, \quad (24)$$

$$w_{i_b,k-1} - w_{i_b,k} = \Delta_z w_{i_b,k}^{ref}. \quad (25)$$

To infer information about the properties of the problem posed here, like stability of the solution and general solution structure, I will employ different combinations of the constraining equations to the linear system (3) to increase the degree of determinacy. The constraints are enforced as hard constraints, by expanding the number of rows of the model matrix \mathbf{M} and the data vector \mathbf{d} (5). Each combination of constraints will be referred to as a strategy, which is then applied to the simulation scenarios (Table 2). The most simple strategy (denoted *Plain* strategy), just considers equations for advection and conservation mass without any additional constraints. It shows that the principle property of the kinematic approach is underdeterminacy. All other strategies are less underdetermined, with the majority being overdetermined systems (Table 2). Only the rather complex MDF-scenario (moderate flow with divergence) will be solved with all strategies and will be used later to discuss the solution properties in detail.

The SVD inversion is implemented with the linear algebra package (LAPACK) routines integrated in MATLAB. As most of the densification takes place in the upper part of the firn column, the inversion covers only the upper 50 m. The inversion grid spans 11×11 nodes, with increments of 500 m and 5 m in the horizontal and vertical, respectively. The SVD grid has a five-fold lower resolution, but its nodes overlap with those from the forward model. The input fields of age and density to the inversion do thus not have to be interpolated. A linear interpolation of the u - and w -reference-velocity fields is carried out to project these values onto the

Table 2. Prescribed additional constraints and system properties for SVD inversion strategies

Strategy	u	$\partial_x u$	$\partial_z u$	M	R	\hat{R}
<i>Plain</i>	–	–	–	162	162	90
<i>Bu</i>	$u_{i,0}$	–	–	172	172	100
<i>Pf</i>	–	–	$0 \forall(i, k)$	242	180	170
<i>Du</i>	–	$\Delta_x u \forall(i, k)$	–	243	180	171
<i>BuPf</i>	$u_{i,0}$	–	$0 \forall(i, k)$	252	180	180
<i>BuDu</i>	$u_{i,0}$	$\Delta_x u \forall(i, k)$	–	253	180	172
<i>DuPf</i>	–	$\Delta_x u \forall(i, k)$	$0 \forall(i, k)$	323	180	179
<i>BuDuPf</i>	$u_{i,0}$	$\Delta_x u \forall(i, k)$	$0 \forall(i, k)$	333	180	179
<i>BuPFW</i>	$u_{i,0}$	–	weighting	172	180	100

Age advection and conservation of mass are considered for all strategies. Strategy coding: *Plain*: no additional constraints; *Bu*: boundary conditions of u at surface prescribed; *Du*: horizontal divergence of u prescribed; *Pf*: plug flow (no shear) prescribed. Constraints are enforced by additional equations to model matrix \mathbf{M} , except for *PfW*, for which plug flow is enforced by matrix weighting. Symbols: $\forall(i, k)$: prescribed for all nodes (i, k) ; dimension of data space M ; dimension of model space $N = 180$ (for all strategies); R mathematical rank; \hat{R} effective (reduced) rank used for inversion.

triplex-staggered grid (Fig. 1). Evidently, the lower resolution and the interpolation will have some influence on the results. However, this effect could be considered equivalent to measurement errors for real data. The influence of data errors on the results will be considered at the end of the following analysis section.

5. Results and Analysis

This section compares the solutions of different strategy for all scenarios. I first illustrate the advantages of SVD-based concepts for comprehensive analyses by investigating the singular-value spectrum (Fig. 3) and resolution matrices (Fig. 4). This is exemplarily discussed for the MDF scenario. Subsequently I discuss the distribution of several norms, which enable us to evaluate the solutions and compare the results for the other scenarios and inversion strategies. The first norm type is the L_2 -norm of the residual and solution vectors, $\|\mathbf{n}'\|$ and $\|\mathbf{v}'\|$, respectively. (We consider the solution of the velocity variation \mathbf{v}' , our main interest, instead of the complete field \mathbf{v} .) The residual norm is a measure of the prediction error of the estimated model parameters \mathbf{v}' in relation to the true (unknown) parameters. As discussed above, the SVD simultaneously minimises these norms to produce the particular solution, with the rank \hat{R} determining the trade-off between residual and solution norm. The second type is the norm of the difference between the reference velocity field (linearly interpolated to the SVD u - and w -grid) and the inverted velocity field ($\|\Delta \mathbf{u}'\| = \|\mathbf{u}'^{ref} - \mathbf{u}'^{sxd}\|$ and $\|\Delta \mathbf{w}'\| = \|\mathbf{w}'^{ref} - \mathbf{w}'^{sxd}\|$), hereafter referred to as velocity difference norms. The latter two quantities provide a

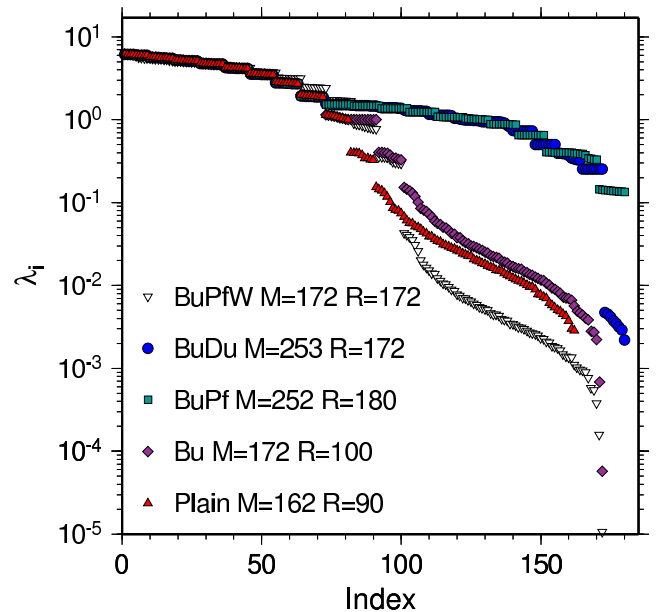


Figure 3. Singular-value spectrum for five inversion strategies applied to the MDF scenario. The strategy *BuPFW* is introduced at the end of this section.

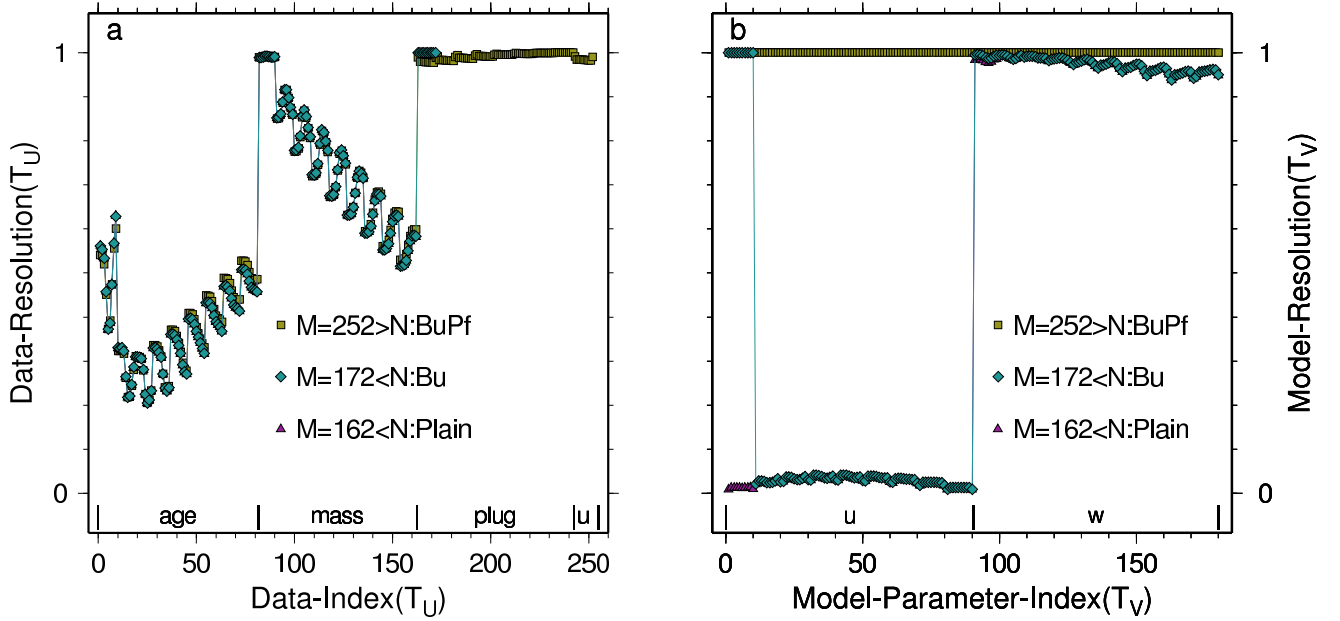


Figure 4. Diagonal of the (a) data and (b) model resolution matrices, \mathbf{T}_U and \mathbf{T}_V , respectively, for the inversion strategies *BuPf*, *Bu*, and *Plain*, given in the legend, applied to the MDF scenario. Components of \mathbf{d}' (data-index, (a)) for *BuPf* correspond to the age equation, conservation of mass, plug-flow constraint, and surface velocity constraint, as indicated on the abscissa. Components of \mathbf{v}' (model-parameter index, (b)) correspond to u and w , respectively, as indicated.

measure of how good a specific inversion strategy performed with respect to the known reference data set.

5.1. Singular-value spectrum

We use four strategies to investigate the structure of the inverted solution for the velocity field of the MDF scenario: the underdetermined and most simple case (*Plain*), the almost determined (*Bu*), and the overdetermined strategies (*BuPf* and *BuD*), using plug flow and divergence, respectively, as constraints. The latter three also constrain the horizontal velocities at the surface.

More than the first third of the ordered singular values, up to about index 72, is basically identical for all strategies (Fig. 3). Beyond this index, the spectra of the overdetermined strategies fall off only slightly, up to about an index of 170. Whereas the singular values of strategy *BuPf* then drop by 50%, those of *BuD* drop almost two orders of magnitude. The underdetermined strategy spectra decrease faster with increasing index. They display two stepwise drops beyond index 72, before continuously decreasing by several orders of magnitudes. The last discrete drop occurs at a singular value of ~ 0.25 . This feature is common to the spectra of all strategies, and is, in general, a typical phenomenon for various problems [Menke, 1989]. The largest difference for all spectra, and the most important ones for the consideration of residual and solution norms, occurs for the smallest about 20–30% of the singular values. Using the untruncated spectra for estimating the model parameters usually results in very small residual norms, equivalent to high resolution, but larger solution norms. The corresponding velocity fields

show very detailed, but unrealistic velocity structures (not shown).

Following experience from different fields where SVD has been employed, I chose the index of the last drop-off as the lower bound of singular values to truncate the continuously and rapidly falling part of singular spectrum. This leads to worse resolution, but smaller solution and also difference norms, and thus more realistic results (Fig. 5). Only for strategy *BuPf*, the full rank is maintained. Although the resulting smallest singular value is comparable for all strategies, the corresponding reduced rank \bar{R} differs significantly (Table 2). This results from the fact that, depending on the solution strategy, the equations show a varying degree of linear independence. The smaller the singular values, the more linearly dependent are the equations.

5.2. Model and data resolution

Another means to partly judge the inversion solution is provided by the resolution matrices. If non-diagonal elements are non-zero, the related main diagonal element < 1 , indicating that this parameter is not fully resolved, i.e. only averages can be determined. I now exemplarily discuss three strategies for the MDF scenario. At full rank, the data are fully resolved for all underdetermined strategies, and the model parameters for all overdetermined strategies. The latter is the case for strategy *BuPf*, for which no reduction of rank was necessary (Fig. 4). For the truncated underdetermined strategy solutions, discussed for the MDF scenario above, the model-resolution matrix \mathbf{T}_V indicates that the horizontal velocities are only poorly resolved (Fig. 4), apart

from those subject to the surface-velocity constraint in the case of *Bu*. The vertical velocities are equally well resolved for both strategies. It will become evident that this is in full accordance with comparison of the actual velocity fields shown in Figure 5 discussed below. Without checking the reference-velocity field it is thus possible to assume that the inverted vertical velocities are more reliable in the underdetermined cases than the horizontal velocities.

For all full-rank underdetermined or truncated overdetermined cases, the data cannot be fitted exactly, giving rise to larger residuals. The diagonal elements of the data-resolution matrices \mathbf{T}_U now indicate that especially the age equations are only poorly resolved for all strategies. The equations for conservation of mass and plug flow are better resolved, though not fully. They show a decreasing resolution trend with depth (larger data index). For strategy *BuPf*, the plug-flow constraint is well resolved, which will be evident in the horizontal velocity structure discussed later. Note that the “oscillations” in data resolution are not arbitrary. The order of diagonal components with index correspond primary to increasing x and secondary to increasing z . The variations thus systematically depend on the position of the underlying equation node, with overall smaller variations in the horizontal than in the vertical. These variations are moreover quasi identical for all three solution strategies. Comparable to the singular spectrum, the model-parameter and data resolution matrices also allow us to judge and improve the quality of the inverted solution by inspecting the residual and solution norm and the singular-value spectrum without requiring a reference-velocity field.

5.3. Inverted versus reference velocity fields

The principle results obtained in the last section are more clearly visible in the actual velocity distribution (Fig. 5). The underdetermined strategy *Plain* does not reproduce the horizontal velocity, but gives a rough idea what the vertical velocity field might look like. In the almost determined case *Bu* the vertical structure is reproduced correctly, but the vertical solution velocities are, however, slightly larger than the reference velocities. The horizontal velocities show the expected divergence clearly only for the surface nodes, i.e. where the horizontal velocities are constraint. The vertical velocities in the overdetermined case are smaller than in the almost determined case and closer the reference values, especially near the surface. As the plug flow is constraint for this strategy and well resolved, the horizontal velocities are now in very good agreement with the reference field (Fig. 5).

5.4. Norm properties for strategies and scenarios

The difference norm for horizontal velocities, $\|\Delta\mathbf{u}'\|$, is very sensitive to the choice of the mean velocity \bar{u} . To provide a similar foundation for all strategies, the mean velocity \bar{u} is always provided as the mean of the reference-velocity field for each scenario, such that only the inverted velocity variations are compared (Table 1). The influence of zero-mean velocities will be discussed below.

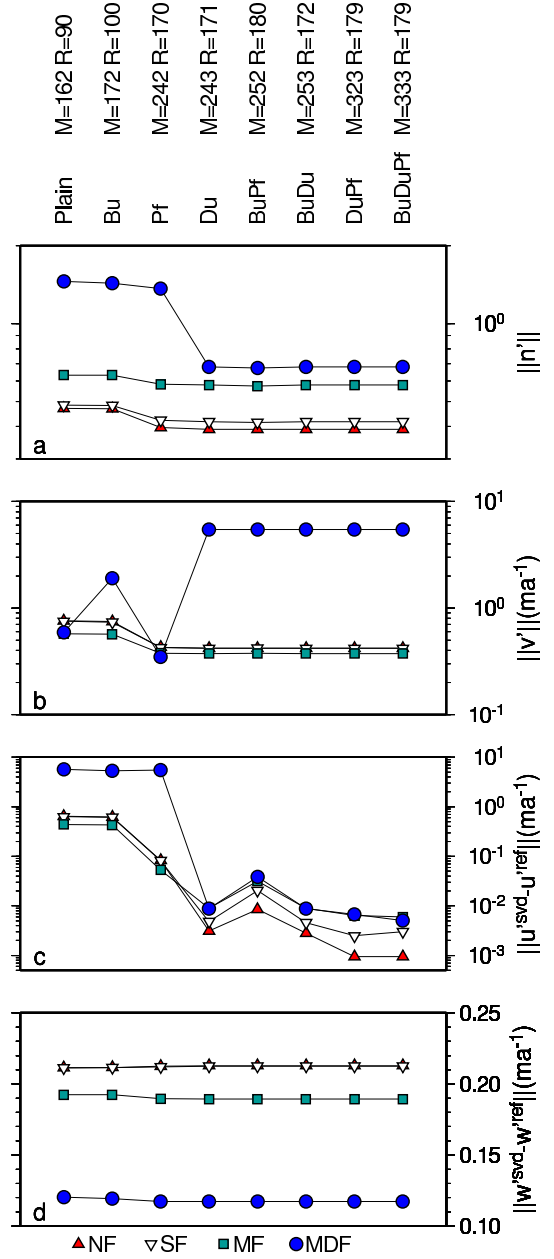


Figure 6. (a) $\|\mathbf{n}'\|$, (b) $\|\mathbf{v}'\|$, (c) $\|\Delta\mathbf{u}'\|$, (d) $\|\Delta\mathbf{w}'\|$ of the different scenarios (Table 1) plotted with the inversion strategies on the abscissa in increasing order of determinacy $M - N$. Note that logarithmic scale is used for $\|\mathbf{v}'\|$ and $\|\Delta\mathbf{u}'\|$. Scenarios are denoted with triangle (NF), downward triangle (SF), square (MF), and circle (MDF).

Ordering the inversion strategies with increasing M (the number of equations) would for full-rank SVD generally illustrate the dependence of the residual norm on determinacy (Fig. 6a). Naturally, for full-rank underdetermined system ($M < N$) the data can be fit exactly, resulting in $\|\mathbf{n}'\| = 0$. For reduced rank, however, the residual norm $\|\mathbf{n}'\|$ increases, but yields a small solution norm $\|\mathbf{v}'\|$ (Fig. 6b). The non-divergent scenarios (NF, SF, MF) provide an almost constant residual and velocity norm for all strategies

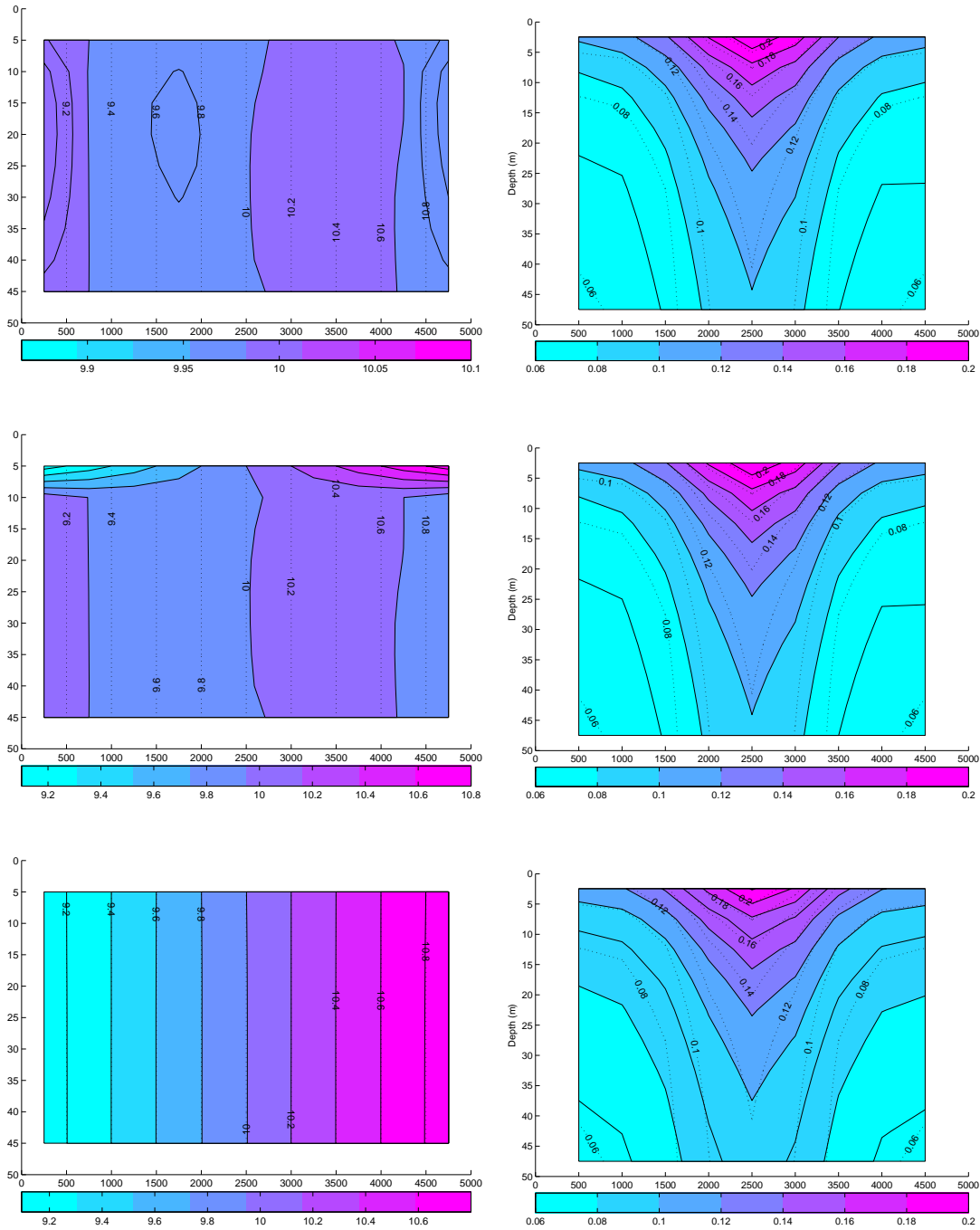


Figure 5. Horizontal (left) and vertical (right) velocity field for the MDF-scenario with strategies *Plain* (top), *Bu* (middle), *BuPf* (bottom). Colormap and solid contours indicate inverted velocity fields, dashed labeled contours indicate reference velocities (units are m a⁻¹). The different horizontal and vertical dimensions of **u** and **v** result from the different grids used (Figure 1).

(at the chosen reduced ranks), with slightly higher values for the underdetermined systems and $\|\mathbf{n}'\|$ ($\|\mathbf{v}'\|$) slightly increasing (decreasing) with the mean velocity. For the divergent scenario (MDF), the residual norm is a factor of two larger for the truncated underdetermined strategies than for the overdetermined strategies. In each group the residual norm is remarkably constant. An exception is the overdetermined strategy constraining plug flow, for which the residual norm is equal to that of the undetermined strategies. The velocity norm $\|\mathbf{v}'\|$ for the MDF scenario spans an order of magnitude, with opposite ratio for under- and overdetermined strategies as for the residual norm, as expected.

More interesting from an application point of view is the residual between input and solution velocities (Fig. 6c and d). The difference norms of horizontal velocities vary much stronger than those of vertical velocities, which are basically independent of strategy. For MDF, $\|\Delta\mathbf{w}'\| \approx 0.12$, for the non-divergent scenarios, $\|\Delta\mathbf{w}'\| \approx 0.19 - 0.21$ (Fig. 6d). Another feature is the similarity of $\|\Delta\mathbf{u}'\|$ and $\|\mathbf{n}'\|$ norm distribution. The two underdetermined strategies as well as *Pf* result in $\|\Delta\mathbf{u}'\|$ 2–4 orders of magnitude larger than for the remaining overdetermined strategies.

Although unlikely, it can occur in reality that no a-priori information on horizontal velocity is available. In those cases, $\bar{u} = 0$ would have to be used. Employing this case for the moderate flow scenarios, the velocity-difference norm remains quasi constant, but the residual norm significantly increases for those strategies that do not incorporate boundary conditions for \mathbf{u} . Without a pinpoint for velocity, the smallest velocities norm result as the solution as a consequence of the minimum-norm property of the SVD. Reducing the rank does not provide remedy in this case.

Likewise, the exceptional norm values for strategy *Pf* result from the missing information about velocity divergence, as only plug flow for \mathbf{u} is constraint. The solution fulfills the plug-flow constraint, but with the smallest norm. That is, rather constant velocities in x -direction. Prescribing divergence instead of plug flow in strategy *Du* yields mathematically an almost identical rank, but moreover the solution contains a certain (constraint) variation of the horizontal velocity. In this case plug flow naturally emerges as the solution with the smallest norm for only small variations in z -direction.

5.5. Weighting vs. full equation for plug-flow constraint

So far all constraints have been enforced as hard constraints by extending the linear system of equations. We now investigate the effect of enforcing the plug-flow constraint by matrix weighting. In addition, the so far neglected model uncertainties (i.e. velocities) will also be included in the weighting matrix \mathbf{F} . The linear system is setup similar to strategy *Bu*, i.e. only boundary conditions of the horizontal velocity at the surface are used as hard constraints. To account for velocity uncertainties the main diagonal of \mathbf{F} is set to 0.9 for \mathbf{u} and \mathbf{w} . Off-diagonal elements are set to 0.1 for \mathbf{u} , allowing some degree of covariance of horizontal veloci-

ties, and set to 0 for \mathbf{w} , implying that the vertical velocities are uncorrelated.

The plug-flow constraint is equivalent to finding the smoothest solution of \mathbf{u} along the vertical, which would usually involve setting the first vertical derivative of \mathbf{u} to zero ($\Delta_z u_{i,k}^{ref} = 0$ in (23)). To relax this condition and allow a larger uncertainty, the relevant off-diagonal elements in \mathbf{F} are set to 0.7. This provides strategy *BuPfW*, an almost determined system with a mathematical rank of 172. Inspection of the singular-value spectrum indicates that only the about 50% largest values are of comparable size for strategies *Bu* and *BuPfW* (Fig. 3). Beyond an index of 72, the singular values of *BuPfW* decrease dramatically, yielding the smallest distribution of all strategies. This implies that the full-rank solution is strongly influenced by the smallest singular values. The prominent gap for singular values around 0.1 is likewise present, as for the other strategies (Fig. 3). Values below this gap are again truncated, as discussed above.

The matrix-weighting strategy *BuPfW* at reduced rank $\hat{R} = 100$ produces similar results as imposing the constraint by equations, as for strategy *BuPf* (Fig. 7). The horizontal velocities are matched very well at all depth for *BuPf* and *BuPfW*, but only poorly for *Bu*, except for the constraint horizontal surface velocities. The vertical velocities for all three strategies are slightly higher than the reference velocities, with decreasing discrepancies with increasing depth.

To demonstrate that the choice made for reducing the rank is a sensible one, based on inspection of the singular spectrum, we now vary \hat{R} over the whole range of possible values and investigate the resulting difference norms for *BuPfW* (Fig. 8). It becomes evident that the velocity-difference norms $\|\Delta\mathbf{u}'\|$ and $\|\Delta\mathbf{w}'\|$ have a somewhat opposing trend. $\|\Delta\mathbf{w}'\|$ is constant at about 3.5 for $\hat{R} \leq 96$, then falls off rapidly to steady values around 0.5 before it rapidly increases for $\hat{R} > 172$. This distribution indicates that for $100 \leq \hat{R} \leq 170$ the vertical reference-velocity structure is approached, although not exactly matched. The distribution of $\|\Delta\mathbf{u}'\|$ slightly decrease from 1.5 to 1 for small \hat{R} . A prominent plateau is present for $40 \leq \hat{R} \leq 105$. In this region the horizontal reference velocities are matched almost perfectly. For larger \hat{R} , $\|\Delta\mathbf{u}'\|$ acceleratingly increases, with largest values present for $\hat{R} = 172$.

Combining both velocity-difference norms, weighted with the squareroot of their mean velocity, a minimum is apparent for $100 \leq \hat{R} \leq 105$. This range corresponds to the final drop in the singular-value spectrum (Fig. 3), chosen above as the truncation criterium. For any \hat{R} within this set the inverted velocities approximate the structure of the reference velocities quite well (Fig. 7). Choosing an \hat{R} outside of this minimum, the vertical velocity deviates more and more from the reference structure for smaller \hat{R} , thus dominating the combined norm, whereas the horizontal velocities dominate the combined norm for larger \hat{R} . For $\hat{R} = 172$, both velocity-component fields are quasi arbitrarily different from the reference fields.

The results indicate that for an underdetermined linear

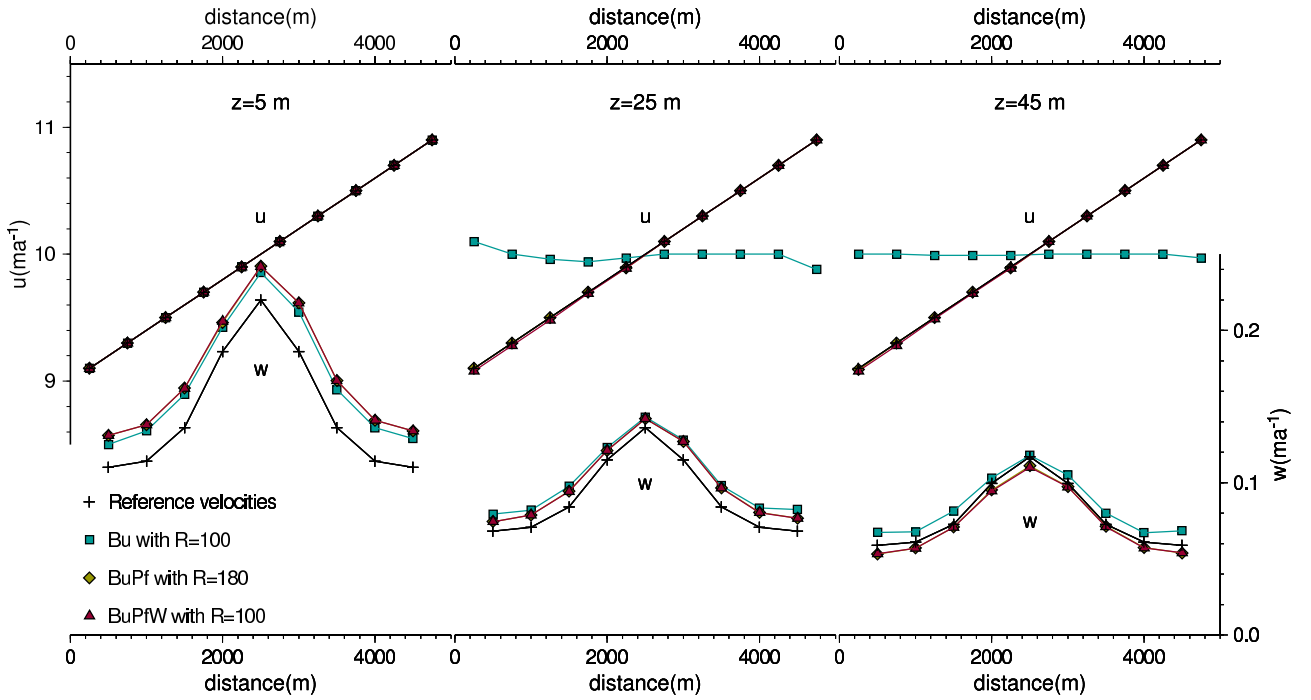


Figure 7. Velocities derived from plug-flow condition imposed by matrix weighting (*BuPFW*) for reduced rank ($\hat{R} = 100$) in comparison to *Bu*, *BuPf* solutions and the reference velocities for the MDF scenario. \mathbf{u} and \mathbf{w} are displayed along horizontal crosssections at three depth, indicated at the top of each panel.

kinematic system, with constraints imposed by matrix weighting, it is possible to find a solution which is close to the true one by choosing a suitable reduced rank. Our choice for truncation made above is based on the structure of the singular-value spectrum, and proved to be the most sensible one. Although we discussed the results only for strategy *BuPFW*, similar analysis for the other strategies yield equivalent findings, demonstrating that the choice of the reduced rank made is indeed a general one.

5.6. Error and covariance estimates

The last point to investigate, fundamental to all inversions, is the solution uncertainty. Input parameters are density ρ and age A . Density measurements along ice cores are very accurate, usually with an uncertainty $< 2\%$. However, our assumption of a lateral homogeneous density distribution might be wrong in some regions. The uncertainty of the age-depth distribution determined from radar surveys depends on numerous factors: the density (for converting radar travel-time to depth), the age estimate from ice cores, transferring the ice-core age to the internal horizons, tracking of individual horizons, and interpolation of the age distribution onto the SVD grid. From analysis of Antarctic field data, Eisen and others [2004] found a maximum error of a couple of percent for the age-depth distribution in firm. In alpine regions, or regions with a lateral inhomogeneous density distribution, this error might be larger.

An error estimate of the model parameters requires knowledge about the data covariance, according to equations (11)

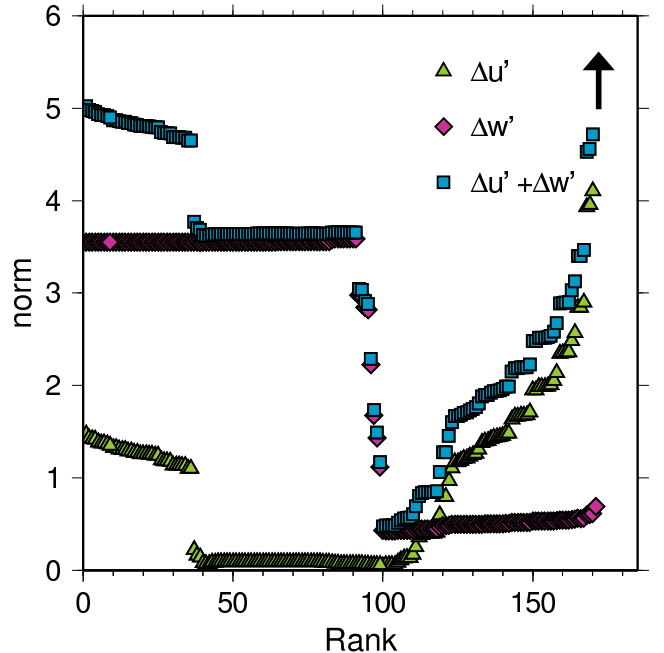


Figure 8. Distribution of $\|\Delta\mathbf{u}'\|$, $\|\Delta\mathbf{w}'\|$, and $\|\Delta\mathbf{u}'\| + \|\Delta\mathbf{w}'\|$ as a function of reduced rank \hat{R} for strategy *BuPFW* for the MDF scenario, with plug flow imposed by matrix weighting. The norms are scaled with the square-root of their mean. Arrow indicates three values of norm 7–14 for $R = 172$.

and (13). For the linear system considered here, uncorrelated uniform variance for the data cannot be assumed, as different physical equations are taken into account. Instead of prescribing an arbitrary data covariance, we perform a Monte Carlo-based estimate of covariances, using perturbed reference velocities, age and density distributions as input to a forward calculation of (5). A total of 10^3 experiments, each of which uses a Gaussian distributed random error of 10% for A , 2% for ρ , and 1% for \mathbf{v}^{ref} results in a distribution of estimated data vectors. From this the corresponding distribution of noise \mathbf{n} follows. Subsequent analysis finally yields an estimate of the noise covariance \mathbf{R}_{nn} . As could be expected from the numerical setup, the different equations are not uncorrelated. Although the main diagonal dominates, secondary diagonals also exhibit significant components. The contribution of the covariance of the nullspace vectors through $\mathbf{R}_{\alpha\alpha}$ to the model uncertainty is neglected, as no a priori information is available.

We exemplarily investigate the model uncertainty again for the solution obtained with strategy *BuPFW* for the MDF scenario. Following (16) and (17), the inversion solves for the velocity variation \mathbf{v} on a background velocity of $\bar{u} = 10 \text{ m a}^{-1}$ and $\bar{w} = 0.1 \text{ m a}^{-1}$. (Note that according to definition (4), the components of \mathbf{v} are arranged with increasing index primary with increasing x and secondary with increasing z). The model uncertainties \mathbf{P}_{vv} are relatively constant at about 0.1 m a^{-1} for all \mathbf{v}' -components (Fig. 9). For horizontal velocity variations \mathbf{u}' , the uncertainty is about one order of magnitude smaller than the largest variation of 1 m a^{-1} . The largest differences between reference and inverted velocities is only about half of the uncertainty estimate. The uncertainty for the vertical velocity variations \mathbf{w}' is on the same order as the actual variation, but again the differences between reference and inverted velocities are much smaller. The estimated model uncertainty can thus be considered a realistic value and an upper error bound, as it contains the observed difference for the system solved here.

The uncertainty of the residuals \mathbf{n} significantly depend on the rank chosen. Generally, for \hat{R} close to the full rank R , the residuals are much larger than their uncertainty. For small \hat{R} , however, as in the present example, the residual uncertainty is an order of magnitude larger than the actual residual. Again, this is the manifestation of the trade-off between resolution and model covariance.

5.7. Improving accumulation estimates

The reader may wonder why it is actually necessary to use a mathematically rather complex inversion scheme under the simplifying assumption of plug flow in firm. If the flow is indeed plug flow, then all information on the horizontal field could be deduced from measurements at the surface. However, determination of accumulation from the age distribution produces significantly different results for inversion solutions and conventional techniques, i.e. by simply calculating the quotient of cumulative mass difference and age difference between to isochrones. The effect of advec-

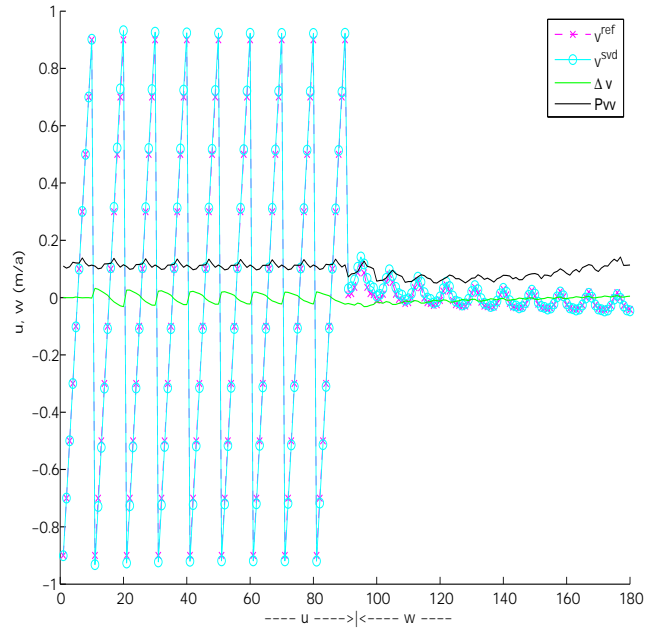


Figure 9. Solution vector \mathbf{v}' for velocity variation, the solution and reference residual vector $\Delta\mathbf{v}'$, and solution uncertainty \mathbf{P}_{vv} for strategy *BuPFW* with rank $\hat{R} = 100$. The components of each vector are ordered primarily with increasing x and secondary with increasing z . Abscissa labels indicate index range for u and w .

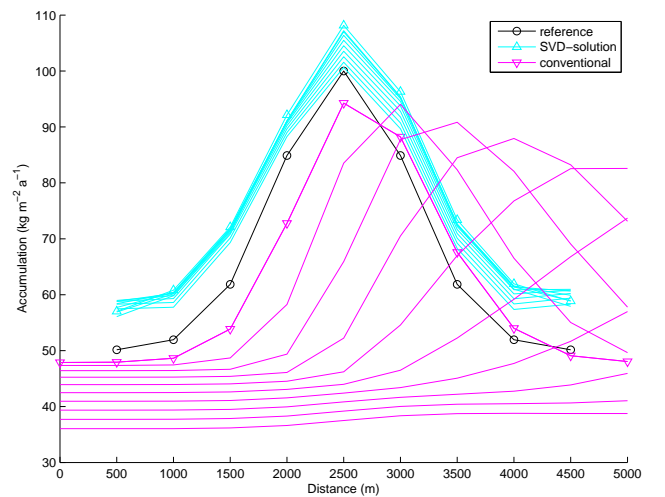


Figure 10. SVD solution vs. conventional accumulation estimates. Inverted accumulation for underdetermined inversion strategy *Bu* calculated from vertical velocities at different depth (cyan); conventional accumulation estimates for the same layer depth (magenta); and accumulation reference (black). Values calculated from the layers nearest to the surface are marked with symbols.

tion on layer architecture for an inhomogeneous accumulation pattern leads to non-intuitive results, as demonstrated by Arcone and others [2005]. Possible misinterpretations are therefore likely for conventional calculations.

Considering the MDF scenario, conventional accumulation estimates from different depths leads to an apparently migrating accumulation pattern (Fig. 10). The accumulation maximum propagates further downstream with increasing depth (age) and the accumulation pattern experiences some broadening. Differences to the reference accumulation are up to 10% for surface layer, but up to 70% for the deeper layers. The *Bu* inversion, on the other hand, yields a stationary accumulation pattern at the surface with a congruent shape. Values are 0–10% larger than the reference at the location of accumulation maximum, and up to 20% and the boundary of the solution domain (Fig. 10). By taking into account a certain amount of advection, even the underdetermined system *Bu* correctly reproduces the accumulation pattern.

Although it is in general possible to correct a conventionally determined accumulation pattern for advection, i.e. the position of the maximum, as long as not interference occurs [Arcone and others, 2005], the broadening pattern cannot be easily overcome. The conventional result could therefore cause a misleading interpretation, like a temporally non-stationary accumulation pattern. This is the fundamental reason for endeavouring an inversion scheme: the separation of temporal and spatial variations in flow and mass balance.

6. Summary

In this paper I investigated the feasibility to invert an age–depth distribution for the velocity field in an advective flow regime in firn by employing a kinematic inversion approach. The inversion was performed by means of a singular-value decomposition of a linear system of equations. The comparison of different flow scenarios and solution strategies with different constraints provides the findings that all kinematic inversion strategies provide a generally stable solution, given that the singular spectrum is adequately truncated; the choice of the reduced rank can be based on objective criteria; for the underlying system of equations, given advection scenarios, and the prescribed spatially inhomogeneous accumulation, the inverted horizontal velocity is much more sensitive to the employed inversion strategy than the vertical velocity;

The amount of information retrieved about the velocity field naturally varies with the degree of determinacy of the underlying linear system. For all strategies, the prescription of surface velocities seems necessary to retrieve small velocity variations superimposed on a mean flow field. Without any quantitative information on horizontal velocity the minimum-norm property of the SVD makes realistic solutions difficult. Instead of extending the linear system with more constraining equations, enforcing additional constraints is equally possible by matrix-weighting.

A detailed investigation of the solution is possible by exploiting the mathematical advantages of the SVD. The solu-

tions were examined in terms of resolution, error estimates, and trade-off of resolution and solution covariance. Estimates of the uncertainty of the solution seem realistic and provide an upper boundary.

The inversion approach is likely applicable to other flow scenarios as well. Two applications to realistic scenarios are obvious. First, interaction of a spatially constant accumulation pattern with a high-velocity flow field could be analysed to infer temporal variations in accumulation by removing the advective components of accumulation estimates. Although the approach presented here assumes a steady-state pattern, larger variations in accumulation derived from isochrones at different depth as those presented above (Fig. 10) could hint to temporally varying accumulation. Second, under certain conditions an accumulation pattern is migrating at a different velocity than the ice. This is for instance the case for megadunes [Frezzotti and others, 2002; Fahnestock and others, 2000]. Using only the surface ice-velocity constraints under such conditions would not result in a realistic pattern of vertical velocity and accumulation. It would be rather reasonable to additionally prescribe flow conditions (e.g. plug flow) and determine the migration velocity of the accumulation pattern relative to the ice surface by inversion.

Possible extensions of the kinematic inversion approach presented here are introduction of more unknown parameters, e.g. using a certain density parameterisation and solving for those parameters as well, and some form of time-dependence. Further attempts towards dynamical equations should be made by inverting parameters for a flow law of firn.

Notation

M	dimension of data space (number of observations)
N	dimension of model space (number of unknowns)
$A, A_{i,k}$	depositional age of particle (tracer)
ρ, ρ_k	density
\dot{b}	accumulation
t	time
x, z	horizontal, vertical spatial coordinate
$\mathbf{r} = (x, z)$	coordinate vector
$u, u_{i,k}$	horizontal velocity component
$w, w_{i,k}$	vertical velocity component
\mathbf{u}, \mathbf{w}	horizontal, vertical velocity field
\mathbf{v}	velocity (model) vector $\in \mathcal{R}^N$ $= (\mathbf{u}^T, \mathbf{w}^T)^T$
\mathbf{d}	data vector $\in \mathcal{R}^M$
\mathbf{n}	residual/noise vector $\in \mathcal{R}^M$
\mathbf{M}	model matrix $\in \mathcal{R}^{M \times N}$
R	mathematical rank of \mathbf{M}
\hat{R}	effective/reduced rank of \mathbf{M}
Λ	singular-value matrix $\in \mathcal{R}^{M \times N}$
Λ_R	submatrix of $\Lambda \in \mathcal{R}^{R \times R}$
λ_i	singular value
\mathbf{U}	data/observation space $\in \mathcal{R}^{M \times M}$

	$= \{\mathbf{U}_R \mathbf{U}_0\}$
\mathbf{V}	model/solution space $\in \mathcal{R}^{N \times N}$
	$= \{\mathbf{V}_R \mathbf{V}_0\}$
\mathbf{U}_R	data range $\in \mathcal{R}^{M \times R}$
\mathbf{V}_R	model range $\in \mathcal{R}^{N \times R}$
\mathbf{U}_0	data nullspace $\in \mathcal{R}^{M \times M-R}$
\mathbf{V}_0	model nullspace $\in \mathcal{R}^{N \times N-R}$
\mathbf{T}_V	model/solution resolution matrix
	$= \mathbf{V}_R \mathbf{V}_R^T$
\mathbf{T}_U	data/observation resolution matrix
	$= \mathbf{U}_R \mathbf{U}_R^T$
\mathbf{R}_{nn}	residual covariance
α	coefficients of data nullspace
$\mathbf{R}_{\alpha\alpha}$	covariance of nullspace coefficients
\mathbf{C}_{vv}	model covariance
\mathbf{P}_{vv}	model uncertainty
\mathbf{P}_{nn}	residual uncertainty
$\mathbf{I}_N, \mathbf{i}_N$	unit matrix $\in \mathcal{R}^{N \times N}$, diagonal of \mathbf{I}_N
$\mathbf{S}_2, \mathbf{W}, \mathbf{F}$	column, row scaling, weighting matrix
$\mathbf{M}, \mathbf{d}, \tilde{\mathbf{v}}$	linear system in scaled space
	$\mathbf{d}, \tilde{\mathbf{v}}$ vectors corresponding to flow-field mean
$\mathbf{d}', \mathbf{v}', \dots$	vectors corresponding to flow-field variations
$\mathbf{u}^{ref}, \mathbf{w}^{ref}$	reference of horizontal, vertical velocity field
$\mathbf{u}^{sdl}, \mathbf{w}^{sdl}$	SVD solution of horizontal, vertical velocity field
$\Delta \mathbf{v}', \Delta \mathbf{u}', \Delta \mathbf{w}'$	residuals of velocity variation (reference–solution)
$\ \Delta \mathbf{u}'\ , \ \Delta \mathbf{w}'\ $	norm of velocity residuals
$\ \mathbf{n}'\ , \ \mathbf{v}'\ $	norm of residual, solution vector
$\langle \mathbf{u} \rangle, \langle \mathbf{w} \rangle$	mean of vectors \mathbf{u}, \mathbf{w}
I, K	number of horizontal, vertical nodes
i, k	horizontal, vertical index
i_b	index of horizontal borehole position
n_u, n_u^x, n_u^z	number of nodes for u : total, x -, z -direction
n_w, n_w^x, n_w^z	number of nodes for w : total, x -, z -direction
$\Delta x, \Delta z$	horizontal, vertical spatial increment
$\Delta_x u, \Delta_z u$	horizontal, vertical difference of u over one spatial increment
$\{c_{i,k}^{\alpha, \dots, \nu}\}$	coefficients of linear system
$x_{min}, x_{max}, z_{max}$	boundaries of x - and z -dimension
b_0, x_σ, x_μ	parameters of accumulation distribution
ρ_0, ρ_i, c_ρ	parameters of density distribution
c_u	parameter of horizontal velocity distribution
∂_i	partial derivative with respect to $i \in \{x, z, t\}$
\mathbf{M}^T	transpose
$\mathbf{\Lambda}^{-1}$	inverse
$\mathbf{W}^{1/2}$	square root (Cholesky decomposition)
δ_{ij}	Kronecker symbol

Appendix:

Cases of determinacy and conditions for existence of nullspaces

$M = N$	just determined
	$\mathbf{V}_0 = \mathbf{U}_0 = \{\}$
$M = N > R$	deficient rank just determined
	$\mathbf{V}_0 \neq \{\}, \mathbf{U}_0 \neq \{\}$
$M > N = R$	full-rank overdetermined
	$\mathbf{V}_0 = \{\}, \mathbf{U}_0 \neq \{\}$
$M > N > R$	deficient rank overdetermined
	$\mathbf{V}_0 \neq \{\}, \mathbf{U}_0 \neq \{\}$
$N > M = R$	full-rank underdetermined
	$\mathbf{V}_0 \neq \{\}, \mathbf{U}_0 = \{\}$
$N > M > R$	deficient rank underdetermined
	$\mathbf{V}_0 \neq \{\}, \mathbf{U}_0 \neq \{\}$

Acknowledgments. Preparation of this work was supported by an “Emmy Noether”-scholarship of the Deutsche Forschungsgemeinschaft grant EI 672/1.

References

- Arcone, S. A., V. B. Spikes, and G. S. Hamilton, 2005, Stratigraphic variation within polar firn caused by differential accumulation and ice flow: interpretation of a 400 MHz short-pulse radar profile from West Antarctica, *J. Glaciol.*, *51*, 407–422.
- Bamber, J. L., R. J. Hardy, and I. Joughin, 2000, An analysis of balance velocities over the Greenland ice sheet and comparison with synthetic aperture radar interferometry, *J. Glaciol.*, *46*, 67–74.
- Clarke, G. K. C., N. Lhomme, and S. J. Marshall, 2005, Tracer transport in the Greenland ice sheet: three-dimensional isotopic stratigraphy, *Quat. Sci. Rev.*, *24*, 155–171.
- Eisen, O., U. Nixdorf, F. Wilhelms, and H. Miller, 2004, Age estimates of isochronous reflection horizons by combining ice core, survey, and synthetic radar data, *J. Geophys. Res.*, *109*, doi:10.1029/2003JB002,858.
- Fahnestock, M. A., T. A. Scambos, C. A. Shuman, R. J. Arthern, D. P. Winebrenner, and R. Kwok, 2000, Snow Megadune Fields on the East Antarctic Plateau: Extreme Atmosphere-Ice Interaction, *Geophys. Res. Letters*, *27*, 3719 – 3722.
- Fiadeiro, M. E., and G. Veronis, 1982, On the determination of absolute velocities in the ocean, *J. Mar. Res.*, *40*, 159,182.
- Frezzotti, M., S. Gandolfi, and S. Urbini, 2002, Snow megadunes in Antarctica: Sedimentary structure and genesis, *J. Geophys. Res.*, *107*, ACL X-1–X-12.
- Frezzotti, M., and others, 2004, New estimations of precipitation and surface sublimation in East Antarctica from snow accumulation measurements, *Climate Dynamics*, *23*, 803 – 813.
- Hindmarsh, R., G. Leysinger-Vieli, M. Raymond, and G. Gudmundsson, 2005, Draping or overriding: The effect of horizontal stress gradients on internal layer architecture in ice-sheets, *J. Geophys. Res.*, p. submitted, doi:10.1029.
- Jacobel, R. W., and B. C. Welch, 2005, A time marker at 17.5 kyrp detected throughout West Antarctica, *Ann. Glac.*, *42*, in press.
- Joughin, I., D. R. MacAyeal, and S. Tulaczyk, 2004, Basal shear stress of the ross ice streams from control method inversions, *J. Geophys. Res.*, *109*.
- Larour, E., E. Rignot, I. Joughin, and D. Aubry, 2005, Rheology of the Ronne Ice Shelf, Antarctica, inferred from satellite radar

- interferometry data using an inverse control method, *Geophys. Res. Letters*, *32*, L05,503, doi:10.1029/2004GL021693.
- Leonard, K. L., R. E. Bell, M. Studinger, and B. Tremblay, 2004, Anomalous accumulation rates in the Vostok ice-core resulting from ice flow over Lake Vostok, *Geophys. Res. Letters*, *31*, L24,401.
- Lüthi, M. P., and M. Funk, 2001, Modelling heat flow in a cold, high-altitude glacier: interpretation of measurements from Colle Gnifetti, Swiss Alps, *J. Glaciol.*, *47*, 314–324, doi.
- MacAyeal, D. R., 1993, A tutorial on the use of control methods in ice-sheet modeling, *Journal of Glaciology*, *39*, 91–98.
- MacAyeal, D. R., R. A. Bindshadler, and T. A. Scambos, 1995, Basal friction of Ice Stream E, West Antarctica, *J. Glaciol.*, *41*, 247–262.
- Menke, W., 1989, *Geophysical Data Analysis: Discrete Inverse Theory*, Academic, San Diego.
- Morse, D. L., 1997, Glacier Geophysics at Taylor Dome, Antarctica, Ph.D. thesis, University of Washington.
- Nerenson, N. A., and E. Waddington, 2002, Isochrones and isotherms beneath migrating ice divides, *J. Glaciol.*, *48*, 95–108.
- Parrenin, F., R. Hindmarsh, and F. Remy, 2005, Analytical solutions for the effect of topography, accumulation rate and flow divergence on isochrone layer geometry, *J. Glaciol., in revision*.
- Richardson, C., and P. Holmlund, 1999, Spatial variability at shallow snow-layer depths in central Dronning Maud Land, East Antarctica, *Ann. Glac.*, *29*, 10–16.
- Richardson-Näslund, C., 2004, Spatial characteristics of snow accumulation in Dronning Maud Land, Antarctica, *Global and Planetary Change*, *42*, 31–43.
- Rotschky, G., O. Eisen, F. Wilhelms, U. Nixdorf, and H. Oerter, 2004, Spatial characteristics of accumulation patterns derived from combined data sets in Dronning Maud Land, Antarctica, *Ann. Glac.*, *39*, 265–270.
- Scales, J. A., M. L. Smith, and S. Treitel, 2001, *Introductory Geophysical Inverse Theory*, Samizdat Press, Golden, White River Junction.
- Schwerzmann, A., M. Funk, H. Blatter, M. Lüthi, M. Schwikowski, and A. Palmer, 2006, A method to reconstruct past accumulation rates in alpine firn regions: A study on Fiescherhorn, Swiss Alps, *J. Geophys. Res.*, *111*, doi:10.1029/2005JF000283.
- Siegert, M. J., R. C. A. Hindmarsh, and G. S. Hamilton, 2003, Evidence for a large surface ablation zone in central East Antarctica during the last Ice Age, *Quaternary Research*, 114–121.
- Viel, A., and A. J. Payne, 2003, Application of control methods for modelling the flow of Pine Island glacier, West Antarctica, *Ann. Glac.*, *36*, 197–204.
- Waddington, E., T. Neumann, M. Koutnik, H. Marshall, and D. Morse, 2004, Inference of accumulation-rate pattern from deep radar layers, *J. Glaciol., in revision*.
- Wunsch, C., 1985, Can a tracer field be inverted for velocity?, *J. Phys. Oceanogr.*, *15*, 1521–1531, doi 10.1175/1520-0485(1985)015.
- Wunsch, C., 1996, *The ocean circulation inverse problem*, Cambridge University Press, Cambridge, New York.
- Xiaolan, W. U., and C. Jezek, 2004, Antarctic ice-sheet balance velocities from merged point and vector data, *J. Glaciol.*, *50*, 219–230.
- Olaf Eisen, Versuchsanstalt für Wasserbau, Hydrologie und Glaziologie (VAW), ETH Zürich, Gloriastr. 37-39, CH-8092 Zürich (e-mail: o Eisen@awi-bremerhaven.de)